Journal of Materials Chemistry A

PAPER

View Article Online
View Journal

Cite this: DOI: 10.1039/c8ta08761j

Atomic layer deposition and first principles modeling of glassy Li_3BO_3–Li_2CO_3 electrolytes for solid-state Li metal batteries†

Eric Kazyak, [a] Kuan-Hung Chen, [b] Andrew L. Davis,[a] Seungho Yu, [a] Adrian J. Sanchez,[a] Jose Lasso,[a] Ashley R. Bielinski,[a] Travis Thompson,[a] Jeff Sakamoto, [abc] Donald J. Siegel [abcd] and Neil P. Dasgupta *[a]

Thin-film lithium solid electrolytes can serve as passivation layers, interfacial coatings, and enable 3D solid-state batteries. Here we present an Atomic Layer Deposition (ALD) process for synthesis of amorphous lithium borate-carbonate (LBCO) films. These films exhibit ionic conductivities up to 2.2×10^{-6} S cm^{-1}, six times greater than previously reported for any ALD solid electrolyte. First principles calculations trace the high conductivity to contributions from enhanced rotational motion of the carbonate and borate anions achieved by precise control of Li and C content by ALD. The high conductivity, coupled with a wide band gap and electrochemical stability window, leads to a total area specific resistance (ASR) of <5 Ω cm^2 for a 100 nm thick electrolyte and an ionic transference number >0.9999 from 0–6 volts *vs.* Li metal. The LBCO ALD solid electrolyte exhibits stability upon exposure to air, and in contact with both Li metal anodes and cathode materials. Thin-film full cells containing Li metal electrodes exhibit high coulombic efficiency for over 150 cycles with no capacity fading. These characteristics make glassy LBCO a promising new material for solid-state Li metal batteries.

Received 9th September 2018
Accepted 28th September 2018

DOI: 10.1039/c8ta08761j

rsc.li/materials-a

Introduction

The demand for batteries with higher energy densities, faster charging times, and longer cycle lives continues to motivate the development of next-generation battery technologies.[1,2] For example, rechargeable Li metal anodes offer the promise of higher specific capacity and energy density than graphite. However, they also present significant challenges to stability, safety, and manufacturing.[3–5] One of the most promising approaches to address these concerns is through the use of solid-state electrolytes (SSEs).[6] If a stable SSE was developed, degradation resulting from electrolyte consumption and SEI formation typical of a liquid electrolyte could be eliminated, enabling long cycle life. Realizing these benefits requires stable solid–solid interfaces between the electrolyte and electrodes. Toward these goals, interest in developing new materials and approaches for fabrication of high-performance solid-state interfaces has surged.[7–9]

To date, formation of stable electrode/electrolyte interfaces during manufacturing and electrochemical cycling remains a challenge for nearly all SSE materials. Oxide materials tend to have limited stability at high rates of operation, particularly at grain boundaries,[10,11] while sulfides are limited by their narrow electrochemical stability window.[6] An ideal solid electrolyte for use with Li metal should either be thermodynamically stable or kinetically stable (after an interphase forms).[12,13] It should also be manufacturable in thin films with scalable processes that are compatible with other materials in the cell, ideally avoiding high temperature and high pressure processing.[7,14]

Due to the limited number of materials that meet these requirements, several studies have employed interfacial layers and/or coatings in combination with bulk solid electrolytes.[8,15–19] There are multiple desirable properties for these interlayers: (1) high ionic conductivity; (2) electrochemical stability against the electrode;[20] and (3) ability to form a thin and conformal layer at the interface to minimize extra mass, while also maintaining a pinhole free film to separate the electrode from the electrolyte.

The most mature technology for fabrication of SSEs for lithium batteries is sputtered lithium phosphorous oxynitride (LiPON), which has been demonstrated to cycle thousands of times with a Li metal electrode in a thin-film battery.[21] Unfortunately, applications of LiPON are limited by the scalability

[a]Department of Mechanical Engineering, University of Michigan, Ann Arbor, MI 48019, USA. E-mail: ndasgupt@umich.edu

[b]Department of Materials Science and Engineering, University of Michigan, Ann Arbor, MI 48019, USA

[c]Michigan Energy Institute, University of Michigan, Ann Arbor, MI 48019, USA

[d]Applied Physics Program, University of Michigan, Ann Arbor, MI 48109, USA

† Electronic supplementary information (ESI) available: Document includes additional experimental data on the composition and phase of the ALD LBCO films, further details on the methods used for electrochemical characterization, and additional results/data from the computational work. See DOI: 10.1039/c8ta08761j

and cost of the sputtering process, and as such, the development of alternate solid electrolytes (oxides, sulfides, *etc.*) and processing methods is of great importance.

An alternative approach to fabricating conformal thin films as either stand-alone electrolytes in thin-film batteries, or as interfacial layers in bulk solid-state batteries, is Atomic Layer Deposition (ALD).[22,23] Unlike physical vapor deposition (PVD) methods, ALD relies on a sequence of self-limiting surface reactions to grow conformal thin films in a non-line-of-sight, layer-by-layer process.[24] This process enables digital/programmable tunability in composition and thickness on complex geometries where traditional thin-film deposition techniques fall short.[25] In addition, many ALD processes can be carried out at relatively low temperatures (often 25–250 °C), which facilitates coating of a wide range of substrate materials (such as Li metal) that would not withstand harsher conditions. Recent advances in Spatial Atomic Layer Deposition (SALD) have increased ALD throughput, reduced manufacturing costs, and are compatible with roll-to-roll processing.[26] For these reasons, many reports have investigated the use of ALD to fabricate materials for energy applications,[27,28] including use in batteries.[22]

Following the pioneering work on ALD interlayers in Li-ion batteries,[29,30] several studies have investigated ALD films as solid electrolytes. Specifically, ALD electrolytes are promising for 3D battery architectures, porous electrode coatings, encapsulation, *etc.*[25] These studies have fabricated a range of oxide, phosphate, and sulfide materials with a wide range of ionic conductivities (10^{-10} to 10^{-7} S cm^{-1}).[31–47] Prior to the present report, the highest reported ionic conductivity in ALD films was in LiPON films: 3.7×10^{-7} S cm^{-1} in solid-state or 6.6×10^{-7} S cm^{-1} in a liquid cell.[31,48] LiPON has been used to make thin-film batteries, and have shown promising electrochemical stability for application in high voltage systems. The recent work by Pearse *et al.* highlights the potential of ALD electrolytes for 3D architectures and demonstrates a proof-of-concept device.[49] One potential limitation of the ALD LiPON films, however, is that the ionic conductivity still lags behind that of sputtered LiPON ($1.8–3.3 \times 10^{-6}$ S cm (ref. 50)) and is well behind that of bulk SSEs (10^{-4} to 10^{-2} S cm^{-1}).[2] For this reason, materials with higher conductivities that maintain wide electrochemical stability windows are of great interest.

Our previous work demonstrated an ALD process for Al-doped $Li_7La_3Zr_2O_{12}$, one of the most promising bulk solid electrolytes.[36] Unfortunately, the ionic conductivity of the amorphous as-deposited films was low ($\sim 10^{-8}$ S cm^{-1}), and uncontrolled morphology evolution during crystallization at elevated temperatures posed additional challenges. As such, ALD films that exhibit high ionic conductivity without requiring high temperature annealing are preferable. In this regard, amorphous/glassy electrolytes are particularly attractive due to the potentially detrimental effects of grain boundaries[11,51] and intergranular Li metal propagation[10] in many crystalline materials.[52]

One promising candidate for an amorphous/glassy ALD solid electrolyte, Li_3BO_3–Li_2CO_3 (LBCO), has been considered for bulk solid electrolytes. First proposed more than four decades ago,[53] the glassy and crystalline phases have been studied as stand-alone solid electrolytes,[54–57] and more recently there have been several reports that use the material as an interfacial layer or in composite electrodes.[58,59] A range of compositions have been reported, varying both lithium content and carbon content to achieve ionic conductivities as high as 10^{-5} S cm^{-1}.[60] Despite these promising properties, there have been no studies to date that use ALD to deposit LBCO.

In this work, an ALD process is demonstrated for glassy LBCO. The film growth is shown to be self-limiting and linear over a range of deposition temperatures. The structure and properties of the film is tuned by varying the deposition and post-treatment conditions, and the electrochemical performance of the films is characterized. The films exhibit higher ionic conductivity than any previously reported ALD film (>10^{-6} S cm^{-1} at 25 °C) with a high ionic transference number of >0.9999, and are shown to be stable over a wide range of potentials relevant for solid-state batteries. The impact of carbon incorporation on structure and diffusivity is calculated with ab initio molecular dynamics (AIMD), providing insight into the mechanism of performance enhancement. Additionally, Density Functional Theory (DFT) calculations of the phase stability and band gap suggest a wide electrochemical stability window and low electronic conductivity. Finally, optimized ALD LBCO films are demonstrated as stand-alone solid electrolytes in thin-film batteries with Li metal electrodes. These cells display stable cycling and exemplify the promise of this process for application both as an electrolyte and as an interfacial layer in solid-state Li metal batteries.

Results and discussion

Process development

The first step in development of an ALD process for LBCO films was identification of precursors. Lithium *tert*-butoxide was selected as the lithium source due to its demonstrated use in other ALD processes.[35,36,44,61] Moreover, by varying the ALD conditions, carbon incorporation into the films can be controlled, which is leveraged in this study to synthesize LBCO films with tunable compositions. Ozone was used as the oxidant[36] to avoid any exposure to moisture, as many battery materials are moisture sensitive.

An obvious choice of boron precursor does not exist. There have been few reports of ALD of binary boron oxide, and its extreme air-reactivity complicates characterization.[62–65] There are two reports of using triisopropyl borate, $[(CH_3)_2CHO]_3B$ (TIB) as a boron source in a ternary B-doped ZnO film, despite the binary process resulting in little to no film growth.[66,67] Therefore, in this study, TIB was selected, as it also has favorable physical properties including being a non-pyrophoric liquid with a vapor pressure of 13 torr at 25 °C.

The LBCO ALD process was first tested with a 1 : 1 ratio of LiO^tBu-O_3 subcycles to TIB-O_3 subcycles. As shown in Fig. 1a, by adding TIB subcycles to an optimized LiO^tBu-O_3 process,[36] pulse saturation was observed using an *in situ* quartz crystal microbalance (QCM). Linear growth with a growth rate of ~0.65 Å per cycle was measured by spectroscopic ellipsometry

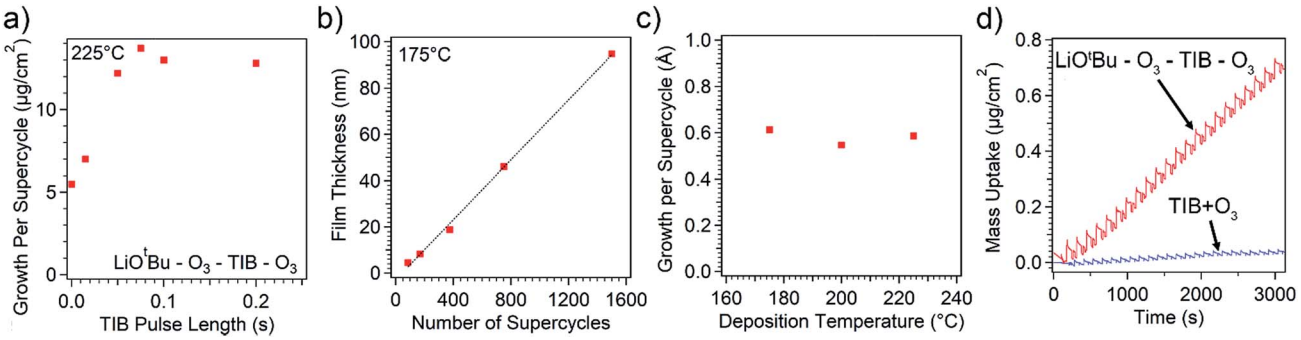

Fig. 1 Characterization of ALD film growth with *in situ* QCM (a and c) and spectroscopic ellipsometry (b and d) showing (a) saturation of growth rate with increasing TIB pulse time, (b) linearly increasing film thickness with number of supercycles, (c) dramatically enhanced growth of the LBCO ALD process compared to the binary boron oxide process, and (d) consistent growth rate across a range of deposition temperatures.

(Fig. 1b), indicating a well-behaved ALD process. The binary TIB-O_3 process was also tested, but very little growth was observed by QCM (<0.1 Å per cycle, Fig. 1c), consistent with the previous report that used water and O_2 plasma as oxidants. Substrate temperatures between 200 °C and 260 °C yielded a relatively consistent growth rate (Fig. 1d).

Film characterization

Further characterization of the growth characteristics of the LBCO ALD process was carried out on etched Si trenches. A ~50 nm ZnO film was deposited *via* ALD to provide a conductive surface to minimize charging and increase contrast between the LBCO film and the substrate. As shown in Fig. 2, the deposited film has uniform thickness along the full height of the trenches. The thickness variation is only ~1.2% along the trench with an aspect ratio of 13. This capability to uniformly coat high aspect ratios is unique to ALD, highlighting the potential of this process for 3-D battery architectures. The ALD film also conformally coats the contours and texture on the sidewalls of the trenches, as it is not a line-of-sight process. This capability could enable the use of less ordered 3-D architectures while maintaining a uniform pinhole-free electrolyte film throughout the structure.

Once the growth conditions had been optimized, the resulting film composition was characterized by XPS. The films were transferred from an Ar filled glovebox to the UHV XPS chamber without air-exposure. As shown in Fig. 3a, the films obtained have a nearly constant Li : B ratio of 3 across the temperature range. The carbon content, however, increases at lower deposition temperatures (Fig. 3c). This is consistent with

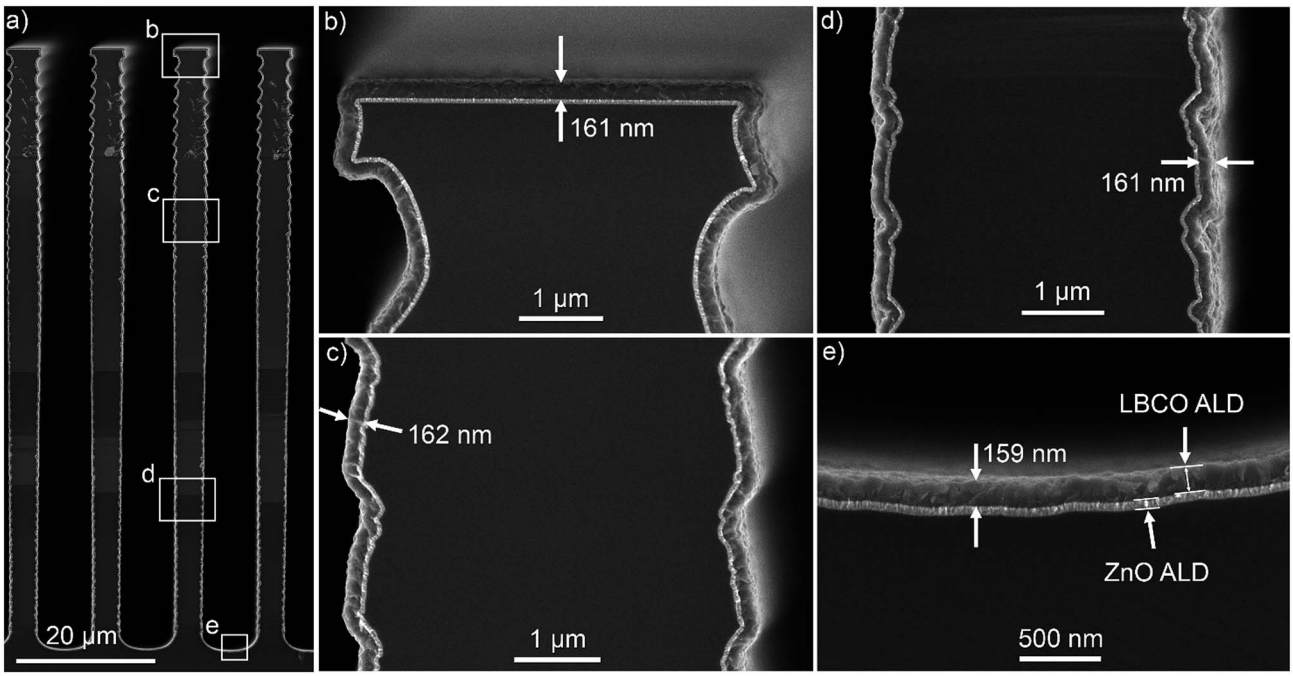

Fig. 2 SEM images of etched Si trenches with ALD ZnO (to reduce charging and increase contrast) and LBCO showing conformality. Full trench shown in (a) with locations along height of trench highlighted and shown in (b–e) with measured thicknesses.

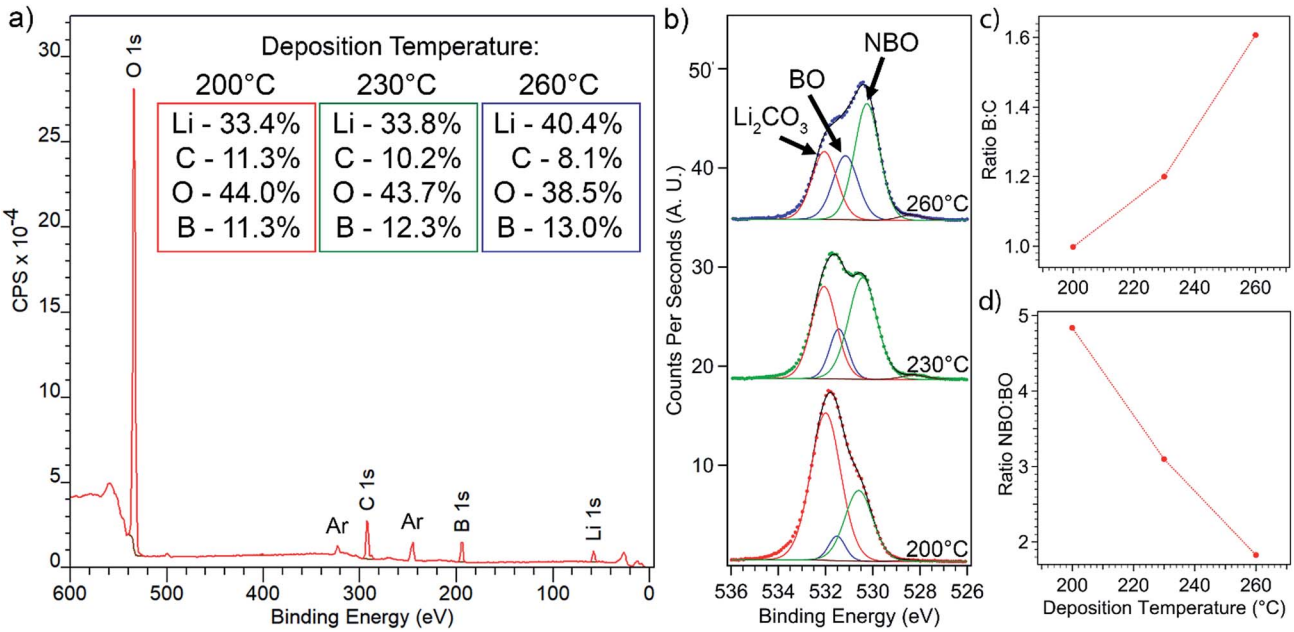

Fig. 3 (a) XPS survey scan for 200 °C deposition temperature with insets showing calculated compositions for each as-deposited film at the three deposition temperatures. (b) XPS O 1s core scan showing changes in oxygen bonding environment with deposition temperature. (c) Plot of the ratio of boron to carbon and (d) the ratio of non-bridging oxygen to bridging oxygen with deposition temperature. All data shown are after 15 minutes of sputtering with Ar ions to remove surface layers.

a previous study of binary processes with LiO^tBu where increasing Li_2CO_3 character was observed at lower deposition temperatures with O_2 plasma.[61] The ability to tune the carbon content relative to boron is of particular interest for achieving high ionic conductivity, as mixtures of Li_2CO_3 and Li_3BO_3 have been shown to have significantly higher ionic conductivity than either of the individual ternary compounds.[53]

The structure of heavily-lithiated borate glasses has been studied previously by both experiment and computation.[54,68] Briefly, as Li_2O is added to the system, the coordination environment of the boron atoms is altered, resulting in a depolymerization in which structures with bridging oxygen (BO) groups are converted to structures with non-bridging oxygen (NBO). This has been correlated with an increase in lithium conductivity, owing to the more open structure and the possible percolation of NBO-rich regions that facilitate faster ion diffusion through the glassy network.[68] In the current study, these phenomena are convoluted with the structural differences that arise due to the presence of Li_2CO_3 in the film. As a result, further analysis of the ALD LBCO films is required to extract the differences in oxygen bonding, particularly the oxygen associated with boron in the glassy structure.

To quantify the presence of NBO in the ALD LBCO films, high-resolution XPS core scans were performed on the O 1s peak. Consistent with prior reports,[7,69] 4 different species can be assigned in Fig. 3b. First, Li_2CO_3 is assigned to the highest binding energy species at 532 eV. The smallest component at the lowest binding energy (~528.5 eV) is assigned to Li_2O, and is present only in trace amounts (<2%) in these films. This leaves the intermediate binding energy peaks that are associated with Li_3BO_3 species. From a previous study of the structure of lithium borate *via* XPS, the higher binding energy species at ~531.4 eV is BO (solid blue line), and the lower binding energy peak at ~530.4 eV is NBO (solid green line).[69] No significant differences were observed in the Li 1s or B 1s core scans (ESI, Fig. S1†).

Due to the proximity of the BO peak to the Li_2CO_3, the C 1s core scans and survey scans were used to validate the deconvolution of the two components (details in the ESI†). Analysis of the fitted O 1s components reveals that the ratio of NBO : BO decreases as deposition temperature increases (Fig. 3d). The tendency to form more NBO at higher temperatures was reported previously based on molecular dynamics calculations.[68] In this case however, it appears that the differences in Li_2CO_3 content have a stronger influence on the oxygen bonding environment than the deposition temperature alone. As NBO species result in higher ionic conductivity, the ability to tune NBO content by varying the ALD processing conditions is of great interest. This observed trend in oxygen bonding environment will be correlated with ionic conductivity in the following section.

Ionic conductivity

To measure the ionic conductivity of the films and evaluate their electrochemical stability, several measurement geometries were used. First, interdigitated platinum electrodes (IDEs) with 5 μm spacing were used for electrochemical impedance spectroscopy (EIS). This in-plane configuration, with two blocking electrodes in the same plane eliminates the need for subsequent deposition of a top electrode, and eliminates the possibility of a short-circuit or an artificially high conductivity due to

a pinhole or thinner region in the film. The geometry of these IDEs and other sample configurations discussed below, including through-plane (TP) measurements on gold substrates, are detailed in Fig. S4.† Both blocking and non-blocking electrode configurations were used to gain a more complete understanding of the film properties.

When studying the temperature-dependent conductivity of the LBCO ALD films, an irreversible increase in conductivity was observed upon heating of the sample. This effect appears as a non-linearity in the heating curve in the Arrhenius plot (Fig. 4a). Upon cooling, the conductivity at 30 °C returns to a higher value than the initial point. Similar behavior was reported previously in sputtered lithium borate films.[60] In the sample shown, this occurs below 100 °C, and very little further increase is observed up to 300 °C. In some samples, a more dramatic increase was observed between 200 °C and 300 °C. A complete mechanistic understanding of this phenomenon is beyond the scope of this work; however, we attribute this behavior to structural changes in the film during annealing. As discussed above, elevated temperatures have previously been shown to result in an increase in NBO, which leads to higher ionic conductivities. We have not observed any crystalline diffraction peaks in the film after this procedure in X-ray diffraction (Fig. S2†), suggesting the film remains amorphous/glassy, however due to the low X-ray scattering cross section of the thin film, we cannot eliminate the possibility of some local ordering.

Because of the improved performance of the film after annealing, all of the subsequent electrochemical data reported, including conductivity, stability, and cycling performance is after the films were annealed to 300 °C with a hold time of 5 minutes. The ionic conductivity as a function of deposition temperature is shown in Fig. 4b. The 200 °C deposition temperature yielded the highest conductivity films. This is the film with the highest amount of carbon (approximately a 1 : 1 B : C ratio), and is the film in which the carbon has the highest proportion of Li_2CO_3 character (ESI†). The incorporation of carbon is desirable owing to its role in increasing ionic conductivity in lithium borate glasses. This is consistent with previous measurements of bulk $Li_{2+x}C_{1-x}B_xO_3$, wherein a maximum ionic conductivity was also observed at a 1 : 1 B : C ratio ($x = 0.5$).[53] Lower deposition temperatures were not tested to avoid potential condensation in the LiO^{t}Bu delivery lines, as the precursor must be heated to 170 °C for sufficient vapor pressure.

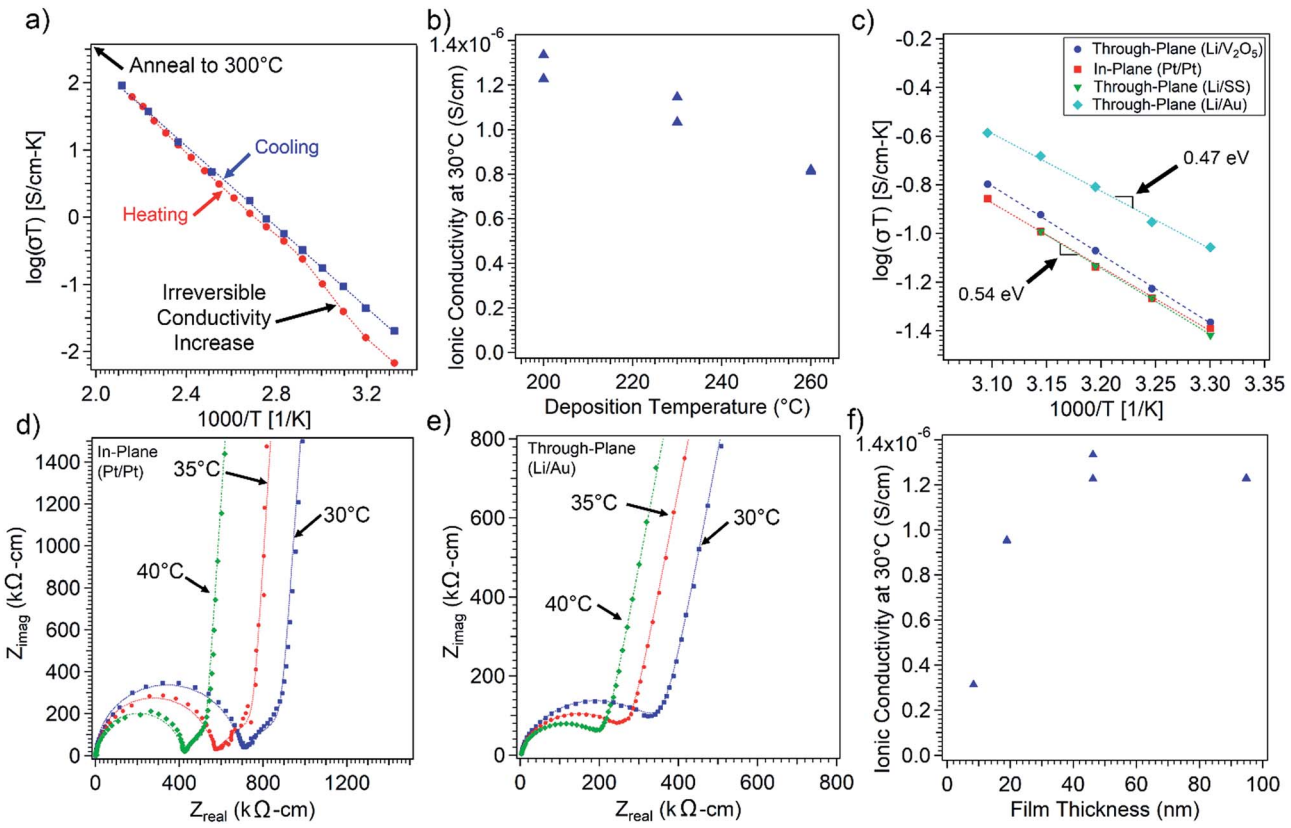

Fig. 4 (a) Arrhenius plot for IDE sample with 44 nm film deposited at 260 °C, showing irreversible increase in conductivity upon annealing in Ar glovebox. (b) Plot showing ionic conductivity as a function of deposition temperature. (c) Arrhenius plot for each of the measurement configurations for the 95 nm film deposited at 200 °C. Nyquist plots for 95 nm film deposited at 200 °C for 30, 35, and 40 °C for (d) Pt interdigitated electrode and (e) through-plane Li *vs.* Au. Experimental data are shown by the point markers and the equivalent circuit fits are shown by the dotted lines. (f) Plot showing the thickness dependence of the ionic conductivity for films deposited at 200 °C, 2 data points are shown for each thickness, but most fall on top of each other and are not visible.

The Nyquist plots for films deposited at 200 °C (after annealing to 300 °C) are shown in Fig. 4d and e for both in-plane IDEs (using Pt–Pt blocking electrodes) and through-plane configurations (using Au–Li blocking-nonblocking electrodes). The equivalent circuits used to fit each of the configurations are shown in Fig. S5.† The general shape is quite similar between all of the conditions, with a semi-circular feature at high frequency and a diffusion tail at low frequencies. The abrupt slope change is due to the thin nature of the electrolyte, and is captured by a modified restricted diffusion element.[36]

The fitted values for the ionic conductivity for each measurement configuration (TP and IDE) are shown in Fig. 4c. The TP-Li/Au cells have an activation energy of 0.47 eV per atom and an ionic conductivity of 2.9×10^{-6} S cm^{-1} at 30 °C (2.23×10^{-6} S cm^{-1} at 25 °C). The TP-Li/SS, TP-Li/V_2O_5, and Pt IDE all give very similar results, with a conductivity of $\sim 1.2–1.4 \times 10^{-6}$ S cm^{-1} at 30 °C and an activation energy of 0.54–0.56 eV per atom ($\sim 1 \times 10^{-6}$ S cm^{-1} at 25 °C). The TP-Li/Au cells gave consistently higher ionic conductivities than the other 3 configurations. We hypothesize that this is a result of improved interfacial contact between the solid electrolyte and the current collector. In other SSE systems, Au is used as an interfacial wetting layer to reduce interfacial impedance.[9] In this case, because the films are so thin and the interfacial impedance cannot be deconvoluted from the bulk by EIS (only one semi-circle is visible), the effect is a drop in total impedance of the cell. This is likely a more accurate estimate of the bulk conductivity of the cells, as the interfaces play a smaller role.

The thickness dependence of the conductivity was studied by depositing films of 4 different thicknesses on the Pt-IDEs. As shown in Fig. 4f, while the thinner films exhibited lower conductivity, the 46 nm and 95 nm thick films had very similar conductivities, suggesting that any thickness dependence of conductivity has plateaued by 46 nm.

To put the ionic conductivity of this LBCO ALD film in the context of previous work, the progression of ALD solid electrolyte development over the past 5 years is shown in Fig. 5. The ionic conductivities of the ALD LBCO films presented here are significantly higher than any previously reported ALD film. The conductivity is comparable to the state-of-the-art sputtered LiPON, which is often reported at $\sim 2 \times 10^{-6}$ S cm^{-1}.[70] With this level of conductivity and the ability to fabricate cells with electrolytes <100 nm thick, the area specific resistance (ASR) is <5 Ω cm^2. This is lower than the interfacial impedance of conventional Li-ion batteries (typically ~10 Ω cm^2), and thus will not be the limiting factor in most applications. Comparing this film to bulk solid-state battery materials, this electrolyte would have the same ASR as a 50 μm thick solid electrolyte with an ionic conductivity of 10^{-3} S cm^{-1}, which is difficult to achieve with traditional processing due to challenges in manufacturing and handling of thin ceramic materials.

Computational simulations

To better understand the differences in behavior of films deposited at different temperatures and with different compositions, AIMD simulations were conducted to study the diffusivity and structure of Li_3BO_3 (LBO) and Li_3BO_3–Li_2CO_3 (LBCO). Fig. 6 and S7 illustrate the calculated mean squared displacement (MSD) and diffusivity for Li-ions in glassy LBO and LBCO. The MSD plots demonstrate that Li-ion displacements in LBCO are larger than those in LBO, suggesting higher ionic mobility in the former phase. This trend is confirmed in the Arrhenius plot, Fig. 6b. The calculated activation energy, E_a, for Li-ion migration in LBCO is 0.31 eV, which is about 25% smaller than the value of 0.40 eV predicted for LBO. Extrapolating the Arrhenius data to room temperature, the AIMD calculations predict that Li-ion diffusivity in LBCO is approximately an order of magnitude larger than in LBO. This trend is consistent with the higher conductivity measured in ALD films deposited at lower temperatures, and therefore with higher Li_2CO_3 content.

Ionic trajectories were analyzed to examine the role of carbon in increasing the Li ion diffusivity in LBCO relative to

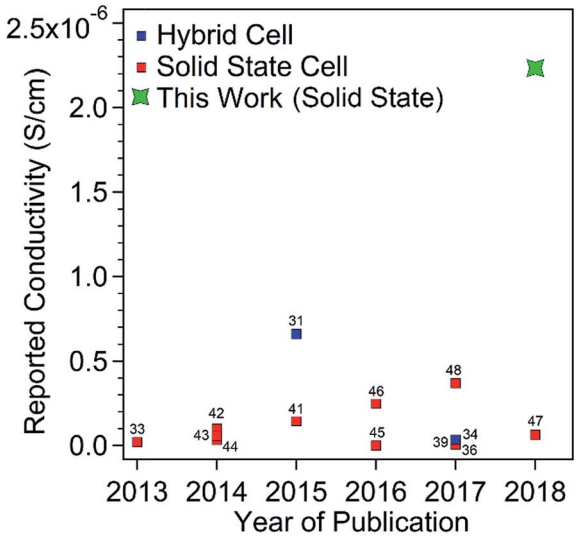

Material System	Conductivity (S/cm)	Reported (K)	Activation (eV)	Reference
LiTaO	2.0E-08	299	0.55	33
LPO	3.3E-08	299	0.51	44
LiAlSiO	1.0E-07	298	0.84	42
LiAlO	5.6E-08	298	0.56	43
LiPON*	6.6E-07	298	?*	31
LiPON	1.5E-07	298	0.55	41
LiAlO	1.0E-10	298	0.8	45
LiAlS	2.5E-07	298	0.48	46
LiSiO	5.7E-09	303	0.8	39
LLZO	1.0E-08	298	0.63	36
LiPON	3.7E-07	298	0.55	48
LiAlF*	3.5E-08	298	?*	34
LiNbO	6.4E-08	303	0.62	47
LBCO	2.2E-06	298	0.47	This Work

*Conductivity measured in liquid cell, no activation energy reported

Fig. 5 Plot and table showing reported ionic conductivity values for ALD films since the first report in 2013.

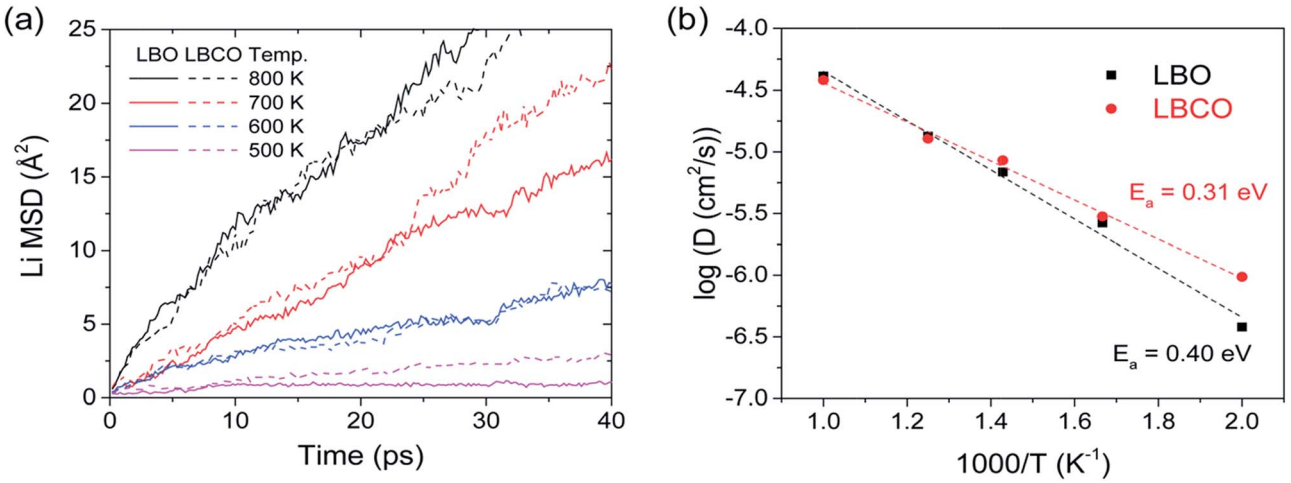

Fig. 6 Calculation of Li diffusivity in glassy LBO and LBCO: (a) Li ion MSD for $T = 500–800$ K, and (b) Arrhenius plots for Li diffusivity over the temperature range 500–1000 K.

LBO. Fig. 7 and S8† plots the ionic probability density isosurfaces for Li and O in LBO and LBCO. The isosurface values shown correspond to twice the average probability, $2P_0$. As expected from the MSD and Arrhenius data (Fig. 6), the probability density isosurfaces for Li (Fig. 7) are more connected and consume a larger fraction of the cell volume than those in LBO (Fig. 7c). Fig. 7b, d and e suggest that dynamical contributions from the carbonate anion in LBCO may explain the relatively higher conductivity exhibited by this phase. For example, Fig. 7b and d compare the probability density for oxygen in LBO and LBCO. The larger volume of the isosurfaces in LBCO imply that oxygen is more mobile in LBCO. Further evidence for a dynamic anionic contribution to cation mobility is shown in Fig. 7e. There it is shown that rotational displacements of O–B and O–C bonds in LBCO are larger than those for O–B in LBO. For example, during a 60 ps AIMD run at 500 K the average anion rotational displacements in LBCO are ~60° for CO_3 and only ~20° for BO_3; these displacements are also much larger than for BO_3 in LBO, whose displacements average only ~10°. These data suggest that the presence of carbonate increases the mobility O coordinated with C or B. We speculate that the more vigorous rotational dynamics of the carbonate and borate complex anions exhibited in LBCO fosters higher mobility in the adjacent Li-ions.

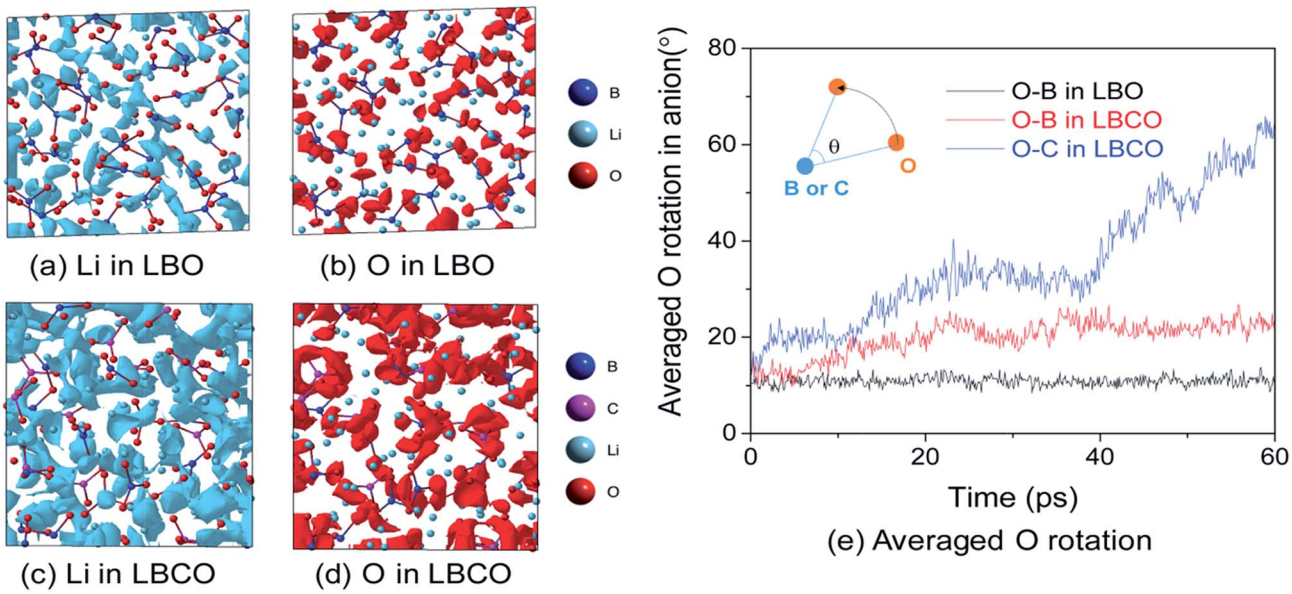

Fig. 7 (a–d) Iso-surfaces of the ionic probability densities evaluated from ionic trajectories calculated over 60 ps AIMD at 500 K. (e) Average oxygen rotational displacements in borate and carbonate anions during AIMD. The iso-surfaces are plotted using an isosurface value of $2P_0$ (P_0 represents the average probability density), for (a) Li in LBO, (b) O in LBO, (c) Li in LBCO, (d) O in LBCO. (e) Averaged oxygen rotational displacements LBO and LBCO during AIMD at 500 K.

Electrochemical stability

In addition to high ionic conductivity, an ideal solid electrolyte would be stable under operating conditions against both the anode and the cathode. In order to test the electrochemical stability of the ALD electrolyte, several experiments were performed. First, the impedance of the electrolyte film was measured over time after evaporation of a Li metal electrode on the surface. Next, cyclic voltammetry was performed on a blocking/non-blocking electrode cell with a Li metal top electrode to examine the current response to an applied voltage. Finally, staircase potentiostatic electrochemical impedance spectroscopy (SPEIS) was used to measure both ionic and electronic conductivity as a function of applied potential.

As shown in Fig. 8a, the cell impedance did not change measurably over 25 days in contact with Li metal. Due to the period of several hours needed to cool and vent the Li evaporator and then begin the test, it is difficult to determine whether there is an initial reaction or not; however, if a reaction does take place, it appears to passivate or become kinetically limited in the initial period of exposure to the Li metal. Regardless of mechanism, the electrolyte remains an ionic conductor with an ionic transference number of ~1 after several weeks in contact with Li metal.

The cyclic voltammetry (CV) scan at 0.1 mV s^{-1} shown in Fig. 8d for a Li *vs.* SS (non-blocking *vs.* blocking) cell shows no peaks in the range between 0 and 3.8 volts *vs.* an evaporated Li counter electrode. This indicates that the ALD electrolyte is stable within this voltage window. This window was chosen as it is similar to the voltage window used for the full cell cycling below. There is a slight deviation as the voltage goes below ~0.2 volts, but the current is still extremely small. The CV to −0.05 volts shown in Fig. 8e demonstrates the ability to plate and subsequently strip Li metal in an all-solid-state cell using this electrolyte. The ratio of anodic to cathodic peak areas is a measure of coulombic efficiency, and in this case the ratio was ~99%, indicating a reversible process.

To further characterize the electrochemical stability window of the LBCO, SPEIS was used. A schematic of this measurement protocol is shown in Fig. S6.† This technique allows measurement of both ionic and electronic conductivity as a function of applied potential. Using these values, the ionic transference number is calculated. The results for the ALD LCBO deposited at 200 °C, shown in Fig. 8c, show very little change in the electronic conductivity as a function of applied potential. The currents measured were very close to the noise floor of the instrument, so the electronic conductivity may be even lower. The ionic conductivity increased slightly as the potential was decreased, and decreased as the potential increased, particularly above ~4 volts. Despite this decrease, the value of the ionic conductivity remained above 10^{-7} S cm^{-1} out to 6 volts, and the

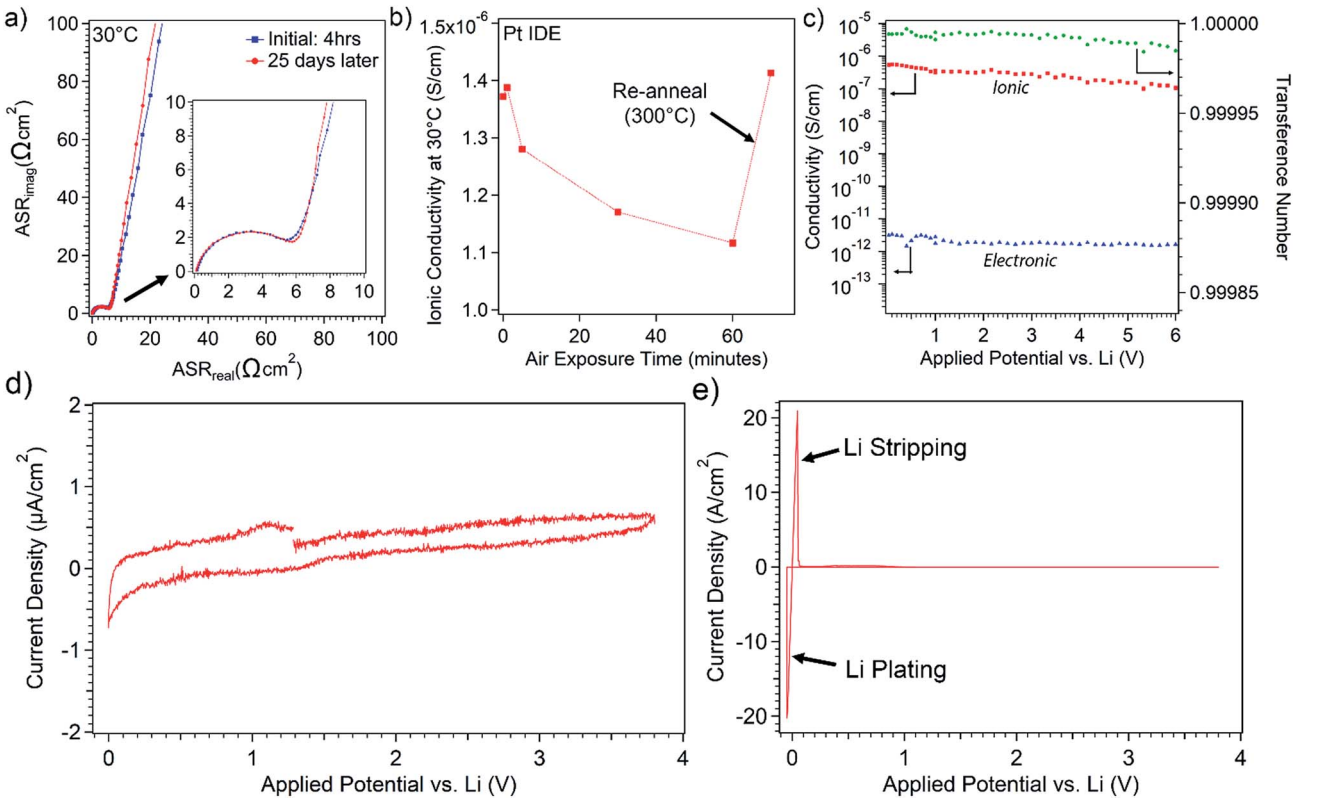

Fig. 8 (a) EIS over time after deposition of a Li metal electrode. (b) Ionic conductivity of an IDE exposed to air and then re-annealed. (c) Staircase Potentiostatic Electrochemical Impedance Spectroscopy (SPEIS) results showing plot of ionic and electronic conductivity as a function of applied potential along with the ionic transference number. (d) CV scan at 0.1 mV s^{-1} showing stability of LBCO in voltage window between 0 and 3.8 volts. (e) Same cell as (b) swept to −0.05 volts showing Li plating and stripping at the blocking stainless steel electrode.

transference number remained above 0.99998. This suggests that the electrolyte could potentially be used with high voltage electrode materials in addition to Li metal anodes.

To gain further insight into the stability of crystalline LBO, amorphous LBCO, and crystalline Li_2CO_3, phase diagram calculations were performed by combining energetics from the present first-principles calculations with data from the Materials Project.[71,72] The calculated phase stabilities as a function of potential with respect to Li/Li^+ are shown in Tables S1–S3.† These calculations indicate LBO is stable between 0.29 and 3.47 V. Similarly, LCO is stable between 1.27 and 4.10 V. Amorphous LBCO is predicted to be a meta-stable phase. The stable phases in the Li–B–C–O quaternary system are predicted to be: Li_2O and LiBC between 0 and 0.45 V, Li_2O, LBO, and C between 0.45 and 1.27 V, and LBO and LCO between 1.27 and 3.47 V.

Table S4 and Fig. S9† report the calculated bandgaps and partial density of states, respectively, for crystalline LBO, amorphous LBO, and amorphous LBCO. The band gaps for amorphous LBO and LBCO are large, 6.2 and 6.0 eV at the HSE06 level of theory, respectively. These values are 0.9 to 1.1 eV smaller than that for crystalline LBO. Due to the large supercells needed to model amorphous phases, an estimate of the bandgap at the more accurate (and expensive) GW level was not attempted for glassy LBCO or LBO. Nevertheless, based on the behavior predicted for crystalline LBO (in going from the HSE06 to HSE06+G_0W_0 levels of theory), we estimate that the band gaps of the amorphous phases are approximately 7.5 eV. Thus, independent of the level of theory, glassy LBO and LBCO are both predicted to be excellent band insulators, consistent with UV-vis spectroscopy measurements shown in Fig. S3.† Their electronically-insulating nature is a desirable property for a solid electrolyte.

Full cell fabrication and cycling

To demonstrate the feasibility of using ALD LBCO as a SSE in a solid-state battery, an ALD-deposited V_2O_5 cathode was deposited prior to the LBCO deposition. Cells with the architecture shown in Fig. 9 were fabricated with a 14.5 nm thick amorphous V_2O_5 and a 95 nm LBCO electrolyte. Amorphous ALD V_2O_5 has previously been demonstrated as a cathode material.[73] Evaporated Li metal was used as an anode. These thin film batteries were tested at varying rates with constant current charging between 1.6 and 3.7 volts.

The cell architecture is shown in the SEM image of a focused ion beam cross-section in Fig. 9a, and schematically in the inset of Fig. 9d. The charge and discharge curves at different rates are shown in Fig. 9b, and the corresponding plot of discharge capacity *vs.* charging rate is shown in Fig. 9c. The cells demonstrate high rate capability, suggesting their use in fast-charging thin-film architectures. Another cell was cycled at 10C for over 150 cycles, and the capacity was still increasing at the end of the experiment as shown in Fig. 9d. This behavior could be due to improved contact at interfaces within the cell or improved transport within the cathode upon cycling. The demonstration of stable cycling in a Li metal thin-film battery is a critical milestone, illustrating that the electrochemical stability of the LBCO electrolyte extends to dynamic cycling conditions. Overall, these results demonstrates the potential of ALD LBCO SSEs, both in 3-D thin film solid-state battery architectures and as interfacial layers in bulk SSEs against Li metal.

Experimental details

Electrolyte deposition

LBCO films were deposited in a Savannah S200 (Ultratech/Cambridge Nanotech, Inc.) integrated with an Ar-filled glovebox. The ability to prevent air-exposure before and after deposition reduces the possibility of reactions leading to undesirable surface reactions that alter the composition and purity of the films prior to characterization. Lithium *tert*-butoxide (97%, Sigma Aldrich) was heated to 170 °C in a stainless steel cylinder and pulse time of 4.0 s, exposure time of 2.0 s, and purge time of 60 s was used. Triisopropyl borate (98%, Sigma Aldrich) was kept at ambient temperature in a stainless steel cylinder and a pulse time of 0.15 s, exposure time of 2.0 s, and purge time of 20 s was used. A carrier gas flow rate of 20 sccm Ultra High Purity Ar was used during purging of the LiO^tBu, 10 sccm during purging of the TIB and ozone, and 5 sccm during precursor exposure. Ozone was produced by a UV ozone generator (Ultratech, Inc.) from Ultra High Purity O_2. Substrate temperatures between 200 °C and 260 °C were used. A lid-integrated *in situ* quartz crystal microbalance was used to monitor film growth.

Film characterization

Ellipsometry was conducted with a Woollam M-2000 with a Si (100) substrate and data were fit with a Cauchy model. An FEI Helios Nanolab 650 SEM/FIB was used for SEM analysis. The etched Si trenches were first Piranha cleaned to remove contaminants. A ~50 nm ZnO film was deposited *via* ALD to provide a conductive surface to minimize charging and increase contrast between the LBCO film and the substrate. Following the LBCO deposition, the structure was cleaved perpendicular to the trenches to reveal the cross-section.

A Kratos Axis Ultra was used for XPS analysis. A monochromated Al source was used. For survey scans, a 160 eV pass energy and 700 × 300 μm sample area. An Ar ion source with 4 kV accelerating voltage and 200 μA extractor current was used for sputtering off any surface film. For high resolution core scans, a pass energy of 20 eV was used, and the C–C peak at 284.8 eV was used for energy calibration. CasaXPS was used for peak fitting with Shirley backgrounds.

Computational modeling

First principles calculations were performed using a plane wave basis set and the projector augmented wave (PAW) method,[74,75] as implemented in the Vienna Ab initio Simulation Package (VASP)[76] Phase stability as a function of electrochemical potential was assessed using the Pymatgen[77] by combining amorphous LBO and LBCO phases from the present DFT

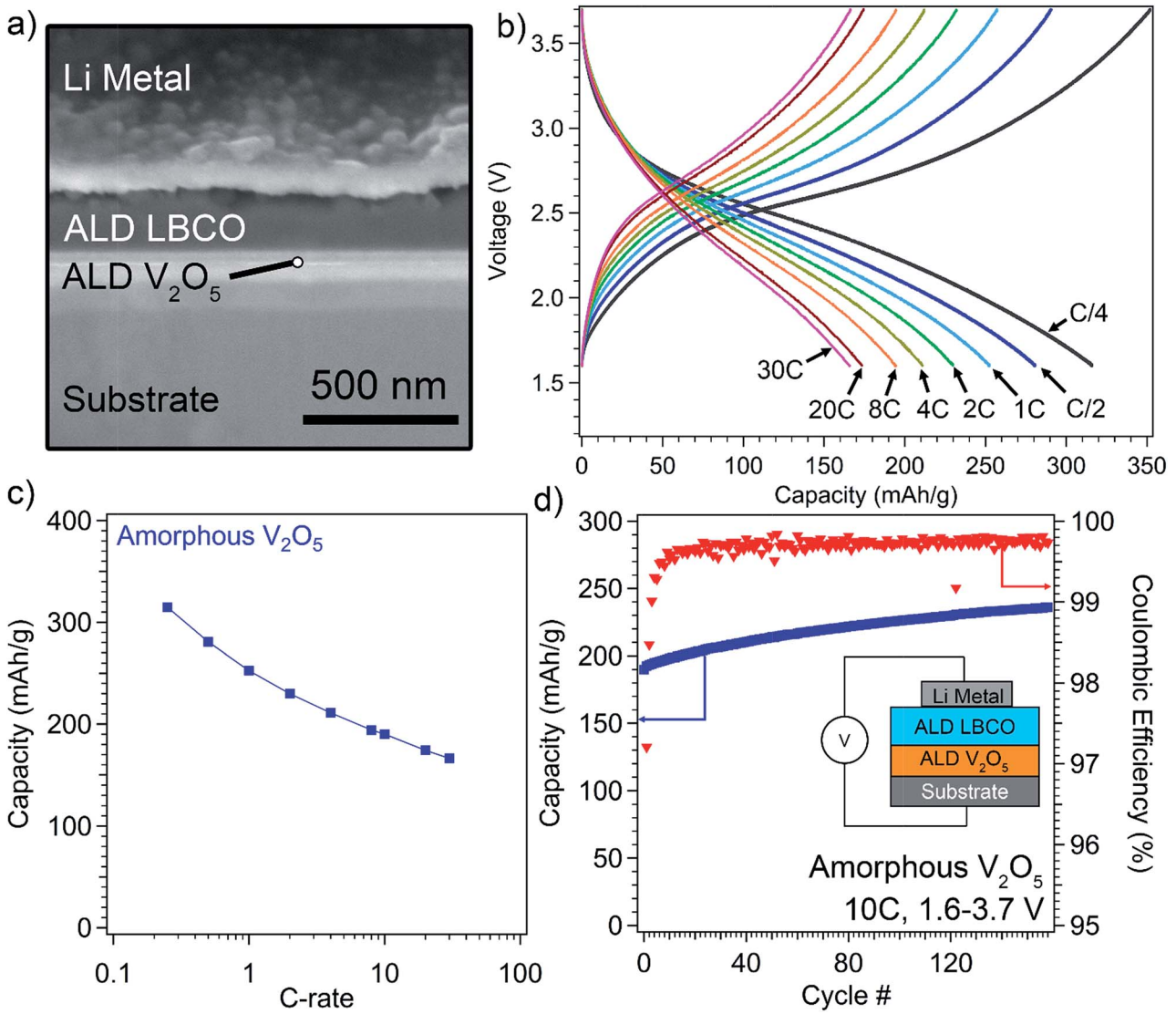

Fig. 9 (a) SEM image of FIB cross-section of full cell stack used in electrochemical measurements. (b) Charge and discharge curves at different rates for full cells, with schematic inset of cell architecture. (c) Discharge capacity at varying rates corresponding for crystalline and amorphous ALD V_2O_5 cathode films (d) plot of discharge capacity and coulombic efficiency for cell cycled at 10C.

calculations with crystalline phases from the Materials Project (MP) database.[78] These data are summarized in the ESI.† Amorphous models for LBO and LBCO glasses were generated using AIMD. The AIMD procedure is described in greater detail in the ESI.† Calculated structural parameters for all of the crystalline and amorphous phases investigated are summarized in Table S5.†

The diffusivity of lithium ions was calculated using AIMD at five temperatures: 1000 K, 800 K, 700 K, 600 K, and 500 K. Mean squared displacement (MSD) data were collected over a 40 ps window at each temperature ranging from 700 to 1000 K, and a with a 100 ps window for the two lower temperatures (500 and 600 K). In all simulations the MSD were recorded after an equilibration time of 5 ps. The diffusion coefficient, D, was obtained by calculating the MSD of Li ions over a time t,

$$D = \frac{1}{2dt}\left\langle [r(t+t_0) - r(t_0)]^2 \right\rangle,$$

where, $d = 3$ is the dimensionality of the system, t_0 is the initial time, and the angled brackets indicate an average over all Li ions.

In addition to calculating diffusion coefficients, the probability densities associated with the magnitudes of ionic displacements were evaluated for both cations and ions. Densities were calculated from ionic trajectories collected over 60 ps at 500 K. Ion positions were sampled using a regular grid of dimension 50 × 50 × 50. Rotational displacements of the borate and carbonate anions were also monitored by calculating changes to the B–O and C–O bond vectors, respectively, from their initial values. Finally, the band gaps of all phases investigated were evaluated using the HSE06 hybrid functional and

G_0W_0 method; these data are reported in Table S4 and Fig. S9 in the ESI.†

Electrochemical characterization

Ionic conductivity. In-plane impedance measurements were conducted using a microprobe station inside of an Ar filled glovebox. ALD films were deposited onto interdigitated platinum electrodes with a 5 μm gap (Dropsens). Each electrode had 250 fingers each 6750 μm in length. Through-plane conductivity measurements were conducted by depositing the electrolyte on a conductive substrate (Au, SS) and then evaporating Li metal through a shadowmask to define the top electrode. A Nexdep evaporator (Angstrom Engineering, Inc.) with a molybdenum crucible was used to deposit a 2 μm Li film. The bottom electrode was exposed by removing the ALD film using 2000 grit sandpaper, and each electrode was contacted using a tungsten needle on a microprobe station (Signatone) inside an Ar glovebox. Potentiostatic electrochemical impedance spectroscopy was carried out using an SP-200 potentiostat (Bio-logic) between 7 MHz and 0.1 Hz with a 10 mV amplitude. Temperature was controlled and monitored with a Watlow EZ-zone controller connected to a Watlow ultramic heater, and temperatures were allowed to stabilize for 5 minutes prior to measurement. Not all samples were directly measured at 25 °C due to the need for active cooling of the glovebox atmosphere and long cooling times necessary to reach that temperature after heating. For samples for which this was not done, the activation energy was used to extrapolate down to 25 °C. Ionic conductivity values were calculated from resistance values fitted to the equivalent circuits found in the ESI.†

Electrochemical stability. Electrochemical stability was tested in the TP-Li/SS cells by several methods. First EIS was conducted periodically to monitor changes in the impedance of the film. Second, cyclic voltammetry was performed with a scan rate of 0.1 mV s^{-1} to observe the flow of current at a range of applied potentials. Finally, staircase potentiostatic electrochemical impedance spectroscopy (SPEIS) was performed in both the positive and negative scan directions from V_{oc}. Since these cells have an open circuit voltage of more than 1 volt, one cell is used for the positive step direction, and another is used for the negative step direction. In this method,[20] a DC bias is applied to the cell for a period of time that allows the current to stabilize, in this case 600 seconds was used. A measure of the DC conductivity was calculated from the average current in the final 100 seconds. Subsequently, potentiostatic EIS is performed about that DC bias potential, and fitting to an equivalent circuit is used to extract an ionic conductivity. A schematic of the applied voltage and current response for this technique is shown in the ESI.† This technique provides both ionic and electronic conductivity as a function of applied potential. This provides a more complete picture of the stability of a solid electrolyte material than cyclic voltammetry.

Full cell fabrication. Full cells were fabricated by depositing V_2O_5 *via* ALD. Vanadium oxytriisopropoxide (VTIP) and water were used as precursors. The deposition was performed in a custom lab-built ALD tool with an Ar carrier gas flow rate of 70 sccm, a pressure of 3.5 torr, and a temperature of 150 °C. Additional Ar gas was used in a "vapor boost" setup to assist in mass transport of the VTIP to the deposition chamber due to the low vapor pressure of the VTIP. The as-deposited V_2O_5 films are amorphous by XRD. The films are then moved into the Ar glovebox and the LBCO solid electrolyte is deposited on top of the V_2O_5. Immediately following this deposition, 2.2 mm diameter Li metal top electrodes were deposited through a shadowmask. The bottom current collector is contacted by sanding away the ALD films, and the top electrode/current collector (Li metal) is contacted with a microprobe, as described above.

Conclusions

This work presents significant advances in several key areas of work relevant to solid-state batteries. First, a new ALD process was developed for fabrication of conformal thin films of the amorphous solid electrolyte lithium borate-carbonate, or LBCO. The degree of Li_2CO_3 incorporation can be tuned by adjusting deposition temperature, which enables control over ionic transport properties. The role of carbon in increasing the conductivity has been elucidated both by first principles calculations and experiments. Increased Li_2CO_3 content increases the ionic mobility of the Li and O in the structure, increasing diffusivity (and ionic conductivity). The films can be grown on high-aspect-ratio 3D structures with excellent uniformity, opening the door to 3D architectures for thin film batteries.

Second, these films exhibited significantly higher ionic conductivity than any previously reported ALD film, while remaining electrical insulators even in very thin films (<100 nm). Ionic conductivities up to 2.23×10^{-6} S cm^{-1} at 298 K were attained, making this material comparable or even superior to sputtered LiPON in terms of ionic transport. This high conductivity coupled with the ability to fabricate cells with <100 nm thick electrolytes means that ASR values of <5 Ω cm^2 can be achieved.

Third, the LBCO films were shown to be stable against anode and cathode materials, and proof of concept devices were fabricated that demonstrate the potential of this material for thin film battery manufacturing. The ionic transport number of the film remained ≈1 from 0–6 volts, and the impedance behavior was stable against a Li metal electrode. In full cells containing Li metal anodes, the ionic conductivity remained high, and excellent cycling stability was observed. The use of computational modelling in this work shows that the wide band gap and stability window in addition to a high diffusivity were indicators of a promising material for application as an electrolyte or interfacial layer. This approach could be used more generally to rapidly screen other material systems to identify promising materials to explore experimentally.

These advances have implications not only for thin-film batteries, as demonstrated here, but could be relevant in next-generation bulk solid-state batteries as interfacial layers and/or protective coatings. The ability to conformally coat a material with high ionic conductivity and good electrochemical stability could enable new approaches, architectures, and

manufacturing strategies for high performance solid-state batteries.

Conflicts of interest

There are no conflicts to declare.

Acknowledgements

The authors acknowledge support from the Advanced Research Projects Association-Energy (ARPA-E), under Award Number DE-AR-0000653. E. K., A. L. D. and A. R. B acknowledge that this material is based upon work supported by a National Science Foundation Graduate Research Fellowship under Grant No. (DGE 1256260). The authors acknowledge the financial support of the University Of Michigan College Of Engineering and technical support from the Michigan Center for Materials Characterization and NSF grants #DMR-0420785 and #DMR-0723032.

Notes and references

1 J.-M. Tarascon and M. Armand, *Nature*, 2001, **414**, 359–367.
2 Z. Zhang, Y. Shao, B. Lotsch, Y.-S. Hu, H. Li, J. Janek, L. F. Nazar, C.-W. Nan, J. Maier, M. Armand and L. Chen, *Energy Environ. Sci.*, 2018, 1945–1976.
3 D. Lin, Y. Liu and Y. Cui, *Nat. Nanotechnol.*, 2017, **12**, 194–206.
4 P. Albertus, S. Babinec, S. Litzelman and A. Newman, *Nat. Energy*, 2018, **3**, 16–21.
5 K. N. Wood, M. Noked and N. P. Dasgupta, *ACS Energy Lett.*, 2017, **2**, 664–672.
6 A. Manthiram, X. Yu and S. Wang, *Nat. Rev. Mater.*, 2017, **2**, 16103.
7 A. Sharafi, E. Kazyak, A. L. Davis, S. Yu, T. Thompson, D. J. Siegel, N. P. Dasgupta and J. Sakamoto, *Chem. Mater.*, 2017, **29**, 7961–7968.
8 X. Han, Y. Gong, K. K. Fu, X. He, G. T. Hitz, J. Dai, A. Pearse, B. Liu, H. Wang, G. Rubloff, Y. Mo, V. Thangadurai, E. D. Wachsman and L. Hu, *Nat. Mater.*, 2016, **16**, 572–579.
9 C. L. Tsai, V. Roddatis, C. V. Chandran, Q. Ma, S. Uhlenbruck, M. Bram, P. Heitjans and O. Guillon, *ACS Appl. Mater. Interfaces*, 2016, **8**, 10617–10626.
10 E. J. Cheng, A. Sharafi and J. Sakamoto, *Electrochim. Acta*, 2017, **223**, 85–91.
11 S. Yu and D. J. Siegel, *Chem. Mater.*, 2017, **29**, 9639–9647.
12 A. Sharafi, S. Yu, M. Naguib, M. Lee, C. Ma, H. M. Meyer, J. Nanda, M. Chi, D. J. Siegel and J. Sakamoto, *J. Mater. Chem. A*, 2017, **5**, 13475–13487.
13 Y. Zhu, X. He and Y. Mo, *ACS Appl. Mater. Interfaces*, 2015, **7**, 23685–23693.
14 J. Schnell, T. Günther, T. Knoche, C. Vieider, L. Köhler, A. Just, M. Keller, S. Passerini and G. Reinhart, *J. Power Sources*, 2018, **382**, 160–175.
15 G. Oh, M. Hirayama, O. Kwon, K. Suzuki and R. Kanno, *Chem. Mater.*, 2016, **28**, 2634–2640.
16 N. Ohta, K. Takada, I. Sakaguchi, L. Zhang, R. Ma, K. Fukuda, M. Osada and T. Sasaki, *Electrochem. Commun.*, 2007, **9**, 1486–1490.
17 S. K. Martha, J. Nanda, Y. Kim, R. R. Unocic, S. Pannala and N. J. Dudney, *J. Mater. Chem. A*, 2013, **1**, 5587.
18 W. C. West, J. F. Whitacre and J. R. Lim, *J. Power Sources*, 2004, **126**, 134–138.
19 A. Sakuda, A. Hayashi, T. Ohtomo, S. Hama and M. Tatsumisago, *Electrochemistry*, 2012, **80**, 839–841.
20 T. Thompson, S. Yu, L. Williams, R. D. Schmidt, R. Garcia-Mendez, J. Wolfenstine, J. L. Allen, E. Kioupakis, D. J. Siegel and J. Sakamoto, *ACS Energy Lett.*, 2017, **2**, 462–468.
21 N. J. Dudney, *Mater. Sci. Eng. B Solid State Mater. Adv. Technol.*, 2005, **116**, 245–249.
22 J. Liu and X. Sun, *Nanotechnology*, 2015, **26**, 24001.
23 L. Ma, R. B. Nuwayhid, T. Wu, Y. Lei, K. Amine and J. Lu, *Adv. Mater. Interfaces*, 2016, **3**, 1600564.
24 S. M. George, *Chem. Rev.*, 2010, **110**, 111–131.
25 J. F. M. Oudenhoven, L. Baggetto and P. H. L. Notten, *Adv. Energy Mater.*, 2011, **1**, 10–33.
26 A. Yersak, Y.-C. Lee, J. Spencer and M. Groner, *J. Vac. Sci. Technol., A*, 2014, **32**, 01A130.
27 J. W. Elam, N. P. Dasgupta and F. B. Prinz, *MRS Bull.*, 2011, **36**, 899–906.
28 N. P. Dasgupta, H.-B.-R. Lee, S. F. Bent and P. S. Weiss, *Chem. Mater.*, 2016, **28**, 1943–1947.
29 Y. S. Jung, P. Lu, A. S. Cavanagh, C. Ban, G. H. Kim, S. H. Lee, S. M. George, S. J. Harris and A. C. Dillon, *Adv. Energy Mater.*, 2013, **3**, 213–219.
30 I. D. Scott, Y. S. Jung, A. S. Cavanagh, Y. Yan, A. C. Dillon, S. M. George and S.-H. Lee, *Nano Lett.*, 2011, **11**, 414–418.
31 A. C. Kozen, A. J. Pearse, C.-F. Lin, M. Noked and G. W. Rubloff, *Chem. Mater.*, 2015, **27**, 5324–5331.
32 C. F. Lin, M. Noked, A. C. Kozen, C. Liu, O. Zhao, K. Gregorczyk, L. Hu, S. B. Lee and G. W. Rubloff, *ACS Nano*, 2016, **10**, 2693–2701.
33 J. Liu, M. N. Banis, X. Li, A. Lushington, M. Cai, R. Li, T. K. Sham and X. Sun, *J. Phys. Chem. C*, 2013, **117**, 20260–20267.
34 J. Xie, A. D. Sendek, E. D. Cubuk, X. Zhang, Z. Lu, Y. Gong, T. Wu, F. Shi, W. Liu, E. J. Reed and Y. Cui, *ACS Nano*, 2017, **11**, 7019–7027.
35 D. J. Comstock and J. W. Elam, *J. Phys. Chem. C*, 2012, **117**, 1677–1683.
36 E. Kazyak, K.-H. Chen, K. N. Wood, A. L. Davis, T. Thompson, A. R. Bielinski, A. J. Sanchez, X. Wang, C. Wang, J. Sakamoto and N. P. Dasgupta, *Chem. Mater.*, 2017, **29**, 3785–3792.
37 A. C. Kozen, C. F. Lin, O. Zhao, S. B. Lee, G. W. Rubloff and M. Noked, *Chem. Mater.*, 2017, **29**, 6298–6307.
38 S. Shibata, *J. Electrochem. Soc.*, 2016, **163**, A2555–A2562.
39 B. Wang, J. Liu, M. Norouzi Banis, Q. Sun, Y. Zhao, R. Li, T. K. Sham and X. Sun, *ACS Appl. Mater. Interfaces*, 2017, **9**, 31786–31793.
40 T. Aaltonen, O. Nilsen, A. Magraso and H. Fjellvag, *Chem. Mater.*, 2011, **23**, 4669–4675.

41 M. Nisula, Y. Shindo, H. Koga and M. Karppinen, *Chem. Mater.*, 2015, **27**, 6987–6993.
42 Y.-C. Perng, J. Cho, S. Y. Sun, D. Membreno, N. Cirigliano, B. Dunn and J. P. Chang, *J. Mater. Chem. A*, 2014, **2**, 9566–9573.
43 J. S. Park, X. Meng, J. W. Elam, S. Hao, C. Wolverton, C. Kim and J. Cabana, *Chem. Mater.*, 2014, **26**, 3128–3134.
44 B. Wang, J. Liu, Q. Sun, R. Li, T.-K. Sham and X. Sun, *Nanotechnology*, 2014, **25**, 504007.
45 Y. Hu, A. Ruud, V. Miikkulainen, T. Norby, O. Nilsen and H. Fjellvåg, *RSC Adv.*, 2016, **6**, 60479–60486.
46 Y. Cao, X. Meng and J. W. Elam, *ChemElectroChem*, 2016, **3**, 858–863.
47 B. Wang, Y. Zhao, M. N. Banis, Q. Sun, K. R. Adair, R. Li, T.-K. Sham and X. Sun, *ACS Appl. Mater. Interfaces*, 2018, **10**, 1654–1661.
48 A. J. Pearse, T. E. Schmitt, E. J. Fuller, F. El-Gabaly, C. F. Lin, K. Gerasopoulos, A. C. Kozen, A. A. Talin, G. Rubloff and K. E. Gregorczyk, *Chem. Mater.*, 2017, **29**, 3740–3753.
49 A. Pearse, T. Schmitt, E. Sahadeo, D. M. Stewart, A. Kozen, K. Gerasopoulos, A. A. Talin, S. B. Lee, G. W. Rubloff and K. E. Gregorczyk, *ACS Nano*, 2018, **12**, 4286–4294.
50 S. Nowak, F. Berkemeier and G. Schmitz, *J. Power Sources*, 2015, **275**, 144–150.
51 J. A. Dawson, P. Canepa, T. Famprikis, C. Masquelier and M. S. Islam, *J. Am. Chem. Soc.*, 2018, **140**, 362–368.
52 L. Porz, T. Swamy, B. W. Sheldon, D. Rettenwander, T. Frömling, H. L. Thaman, S. Berendts, R. Uecker, W. C. Carter and Y. M. Chiang, *Adv. Energy Mater.*, 2017, **7**, 1–12.
53 R. D. Shannon, B. E. Taylor, A. D. English and T. Berzins, *Electrochim. Acta*, 1977, **22**, 783–796.
54 E. E. Horopanitis, G. Perentzis, A. Beck, L. Guczi, G. Peto and L. Papadimitriou, *J. Non-Cryst. Solids*, 2008, **354**, 374–379.
55 T. Okumura, T. Takeuchi and H. Kobayashi, *Solid State Ionics*, 2016, **288**, 248–252.
56 K. Nagao, A. Hayashi and M. Tatsumisago, *J. Ceram. Soc. Jpn.*, 2016, **124**, 915–919.
57 E. E. Horopanitis, G. Perentzis, E. Pavlidou and L. Papadimitriou, *Ionics*, 2003, **9**, 88–94.
58 K. Park, B. C. Yu, J. W. Jung, Y. Li, W. Zhou, H. Gao, S. Son and J. B. Goodenough, *Chem. Mater.*, 2016, **28**, 8051–8059.
59 H. Zhang, S. Hao and J. Lin, *J. Alloys Compd.*, 2017, **704**, 109–116.
60 F. Berkemeier, M. R. S. Abouzari and G. Schmitz, *Phys. Rev. B: Condens. Matter Mater. Phys.*, 2007, **76**, 1–9.
61 A. C. Kozen, A. J. Pearse, C.-F. Lin, M. A. Schroeder, M. Noked, S. B. Lee and G. W. Rubloff, *J. Phys. Chem. C*, 2014, **118**, 27749–27753.
62 M. Putkonen and L. Niinistö, *Thin Solid Films*, 2006, **514**, 145–149.
63 W.-H. Kim, I.-K. Oh, M.-K. Kim, W. J. Maeng, C.-W. Lee, G. Lee, C. Lansalot-Matras, W. Noh, D. Thompson, D. Chu and H. Kim, *J. Mater. Chem. C*, 2014, **2**, 5805.
64 B. Kalkofen, V. Mothukuru, M. Lisker and E. Burte, *ECS Trans.*, 2012, **45**, 55–67.
65 T. E. Seidel, J. W. Elam, M. I. Current and A. U. Mane, *Proc. Int. Conf. Ion Implant. Technol.*, 2017, pp. 9–12.
66 H. A. Gatz, D. Koushik, J. K. Rath, W. M. M. Kessels and R. E. I. Schropp, *Energy Procedia*, 2016, **92**, 624–632.
67 D. Garcia-Alonso, S. E. Potts, C. A. A. van Helvoirt, M. A. Verheijen and W. M. M. Kessels, *J. Mater. Chem. C*, 2015, **3**, 3095–3107.
68 C.-P. E. Varsamis, A. Vegiri and E. I. Kamitsos, *Phys. Rev. B: Condens. Matter Mater. Phys.*, 2002, **65**, 104203.
69 D. A. Hensley and S. H. Garofalini, *Appl. Surf. Sci.*, 1994, **81**, 331–339.
70 F. Xu, N. J. Dudney, G. M. Veith, Y. Kim, C. Erdonmez, W. Lai and Y. M. Chiang, *J. Mater. Res.*, 2010, **25**, 1507–1515.
71 A. Jain, S. P. Ong, G. Hautier, W. Chen, W. D. Richards, S. Dacek, S. Cholia, D. Gunter, D. Skinner, G. Ceder and K. A. Persson, *APL Mater.*, 2013, **1**, 11002.
72 S. P. Ong, L. Wang, B. Kang and G. Ceder, *Chem. Mater.*, 2008, **20**, 1798–1807.
73 K. Geryl, Atomic layer deposition of vanadium oxides for lithium-ion batteries, Master's Dissertation, 2014, vol. 153.
74 P. E. Blöchl, *Phys. Rev. B: Condens. Matter Mater. Phys.*, 1994, **50**, 17953–17979.
75 D. Joubert, *Phys. Rev. B: Condens. Matter Mater. Phys.*, 1999, **59**, 1758–1775.
76 G. Kresse and J. Furthmüller, *Phys. Rev. B: Condens. Matter Mater. Phys.*, 1996, **54**, 11169–11186.
77 S. P. Ong, W. D. Richards, A. Jain, G. Hautier, M. Kocher, S. Cholia, D. Gunter, V. L. Chevrier, K. A. Persson and G. Ceder, *Comput. Mater. Sci.*, 2013, **68**, 314–319.
78 A. Jain, G. Hautier, C. J. Moore, S. Ping Ong, C. C. Fischer, T. Mueller, K. A. Persson and G. Ceder, *Comput. Mater. Sci.*, 2011, **50**, 2295–2310.